Nucleate boiling enhancement by structured surfaces with distributed wettability-modified regions: A lattice Boltzmann study

W. X. Li [1], Q. Li [1, *], Y. Yu [1], and Kai H. Luo [2]

[1] *School of Energy Science and Engineering, Central South University, Changsha 410083, China*

[2] *Department of Mechanical Engineering, University College London, London WC1E 7JE, United Kingdom*

*Corresponding author: qingli@csu.edu.cn

Abstract

In this paper, we conceive a novel pillar-structured surface for enhancing nucleate boiling heat transfer, namely a pillar-structured surface with distributed wettability-modified regions on the top of each pillar. A three-dimensional thermal multiphase lattice Boltzmann model with liquid-vapor phase change is employed to investigate the boiling performance on the pillar-structured surface with distributed wettability-modified regions and the associated mechanism of nucleate boiling heat transfer enhancement. According to the distribution of the wettability-modified regions, the bubble dynamics on the newly conceived pillar-structured surface can be classified into three regimes, i.e., regimes I, II, and III, among which the regime II shows relatively better boiling performance than the other two regimes due to the synergistic effects of surface structure and mixed wettability. It is found that in the regime II the bubbles nucleated at the wettability-modified regions do not coalesce with each other, which therefore elongates the length of the triple-phase contact lines on the pillar top in comparison with the pillar-structured surface with a unified wettability-modified region. Meanwhile, in the regime II the bubbles on the pillar top receive a strong bubble-wake effect supplied by the bubbles generated at the bottom substrate, which shortens the bubble growth cycle and promotes the departure of the bubbles on the pillar top, and also reduces the area of dry spots on the pillar top. The influences of the pillar width and the width of the wettability-modified regions are also studied. It is shown that the best boiling performance is always achieved in the cases that fall into the regime II.

1. Introduction

Boiling heat transfer has been widely utilized in various thermal energy dissipation systems and industrial fields such as nuclear power reactors [1], chemical engineering [2], refrigeration [3], and electronic devices [4]. Owing to the large latent heat consumption of liquid-vapor phase change, boiling heat transfer provides a much higher heat removal capacity than that of single-phase thermal convection. In the past decades, an enormous amount of experimental and numerical studies have been conducted to investigate the boiling mechanism and explore approaches to enhance the nucleate boiling heat transfer. Generally, the surface structure [5], wettability [6], working fluid [7], and liquid capillarity [8] may be modified to improve the boiling performance of a heating surface. In particular, the surface structure and wettability have been recognized as the key parameters influencing the boiling performance [9, 10].

In the literature it has been well revealed that decreasing the surface wettability of a heating surface can trigger more bubbles because of reducing the energy barrier of liquid-vapor phase change [11, 12]. However, a hydrophobic surface with poor wettability usually leads to a lower value of critical heat flux than that of a hydrophilic surface. Conversely, the hydrophilic surface, which has a higher liquid affinity ability, can delay the occurrence of critical heat flux but suppress the bubble nucleation [13, 14]. To break through these limitations, the heating surfaces with mixed wettability combining hydrophobicity and hydrophilicity have attracted much attention in recent years. It has been found that taking the advantages of both of the hydrophobic and hydrophilic properties may simultaneously improve the critical heat flux and the heat transfer coefficient [10, 15, 16].

Moreover, the surface structure also plays a very important role in boiling heat transfer. Compared with a plain surface, a structured surface can offer more activated nucleation sites for enhancing the nucleate boiling heat transfer [17]. Besides, the critical heat flux can also be improved by the capillary wicking supplied by a roughly structured surface [18]. However, a structured surface with too large roughness may result in horizontal bubble coalescence and form a vapor film that covers the heating surface, which will reduce the critical heat flux [19].

By combining the effects of surface structure and wettability, Jo *et al*. [20] have created a heterogeneous wetting surface through fabricating wetting patterns onto the tops of microstructures. They found that the heterogeneous wetting surface with microstructures can interrupt the expansion and coalescence of bubbles and hence enhance the boiling heat transfer performance. Moreover, the synergistic effects of surface structure and mixed wettability have also been investigated by Shen *et al*. [21] and Zhang *et al*. [22]. Shen *et al*. [21] applied the chemical deposition method to fabricate a hybrid wetting surface with square pillars on a millimeter scale. They revealed that the hybrid wetting mode is a significant factor influencing the boiling performance and the mode that consists of a hydrophobic pillar top and a hydrophilic bottom surface is the most effective one among the investigated modes. Furthermore, Zhang *et al*. [22] experimentally demonstrated that the combination of microstructures and hydrophobicity can supply more bubble nucleation sites and reduce the energy barrier of liquid-vapor phase change.

When a vapor bubble is detached from a hydrophobic surface, it is usually separated into two parts after the bubble necking, i.e., a departure bubble and a residual vapor bubble [10, 11, 23-25]. The residual vapor bubble remains on the heating surface as a nucleus of the next boiling cycle, which generates a string of bubbles with no waiting time. Nevertheless, continuous bubbles may preclude the liquid from rewetting the heating surface and result in the formation of dry spots. Recently, Surtaev *et al*. [23] have investigated this phenomenon using the high-speed video as well as the infrared thermography. They observed that the liquid microlayer ceases to exist on a hydrophobic surface underneath the residual vapor bubble. Besides, Kangude and Srivastava [24] studied the spatio-temporal temperature distribution of a hydrophobic surface during a boiling process. It is found that the local temperature of the central region underneath the residual bubble is higher than that of the surrounding regions and the heat transfer mainly occurs at the triple-phase contact lines, which indicates that the triple-phase contact lines play an important role in the boiling heat transfer of a hydrophobic surface.

Although numerous experiments have been carried out to investigate the boiling phenomena, the enhancement mechanism of boiling heat transfer has not been well understood due to the complexity of

boiling processes. With the rapid development of high-performance computational technology, computational fluid dynamics (CFD) has become very important in fluid flow and heat transfer studies. Compared with experiments, numerical simulations can provide more details of boiling processes to promote the understanding of the mechanism of boiling heat transfer [26]. In the past three decades, the lattice Boltzmann (LB) method, which originated from the lattice-gas automata method, has been developed into a very attractive alternative to conventional numerical methods [27, 28]. This method has been proven to be very suitable for studying multiphase and multicomponent systems [29, 30] where the interfacial dynamics and phase transition are present.

In recent years, the LB method has been extensively employed to simulate boiling phenomena. Specifically, this method has been applied to investigate the boiling performances of heating surfaces with mixed wettability, including both flat and structured surfaces. For example, Gong and Cheng [31] have investigated the boiling heat transfer on a flat surface with mixed wettability using the LB method. They numerically demonstrated that adding hydrophobic spots on a flat hydrophilic surface can promote bubble nucleation and reduce the nucleation time. Besides, Li *et al*. [32, 33] have used the LB method to study the boiling performance of a hydrophilic-hydrophobic structured surface, which is textured by square pillars consisting of hydrophobic tops and hydrophilic sidewalls. They found that the hydrophobicity of pillar tops offers more nucleate sites and can reduce the wall superheat required for boiling onset. In addition, Ma *et al*. [25] have numerically investigated four types of micro-pillar heat sinks with different wettability patterns. Recently, Li *et al*. [34] numerically proposed an improved type of pillar-structured surface with mixed wettability to explore the joint effects of surface structure and wettability for enhancing the nucleate boiling heat transfer. It was found that the width of wettability-modified region on the pillar top has an important influence on the boiling performance of a structured surface with mixed wettability. Moreover, using the LB method, Lee *et al*. [35] have investigated the influences of triple-phase contact lines on the boiling performance of a flat hydrophilic surface patterned with cross-shaped hydrophobic dots. Through characterizing the shapes of cross dots by different aspect ratios, they found that the heat flux increases

with the increase of the aspect ratio owing to elongating the triple-phase contact lines.

From the aforementioned experimental and numerical studies, it can be found that a structured surface that combines hydrophobicity and hydrophilicity is a very useful option for enhancing boiling heat transfer. Nevertheless, as previously mentioned, the residual vapor that remains on the hydrophobic region may preclude the fresh liquid from rewetting the heating surface, which probably causes the formation of dry spots and high temperatures at the hydrophobic region. On the other hand, the triple-phase contact lines distributed on the hydrophobic region usually show the lowest temperature and the highest heat flux [24, 36]. Therefore, elongating the triple-phase contact lines may be a useful strategy for further enhancing the boiling performance of a structured surface with mixed wettability. Based on this consideration, in the present work we numerically conceive a novel pillar-structured surface with distributed wettability-modified regions on the top of each pillar. With this design, the length of the triple-phase contact lines can be elongated without reducing the total area of the wettability-modified regions.

To the best of our knowledge, such a pillar-structured surface with distributed wettability-modified regions on each pillar top has not been previously studied, neither experimentally nor numerically. A three-dimensional (3D) thermal multiphase LB model with liquid-vapor phase change will be adopted to investigate the boiling performance of the pillar-structured surface with distributed wettability-modified regions. The rest of the present paper is organized as follows. The 3D thermal multiphase LB model with liquid-vapor phase change is briefly introduced in Section 2. Numerical simulations of boiling heat transfer on the pillar-structured surface with distributed wettability-modified regions are carried out in Section 3, with the focus being placed on the bubble dynamics and the associated mechanism of the pillar-structured surface with distributed wettability-modified regions for enhancing nucleate pool boiling. Finally, a brief summary is given in Section 4.

2. Numerical method

In this section, the 3D thermal multiphase LB model with liquid-vapor phase change utilized in the

present study is briefly introduced. Historically, the LB method originated from the lattice-gas automata method [27, 28], but it was later demonstrated that the LB equation can be viewed as a special discretized from of the Boltzmann equation in the kinetic theory with a certain collision operator, such as the Bhatnagar-Gross-Krook (BGK) [37, 38] collision operator or the multiple-relaxation-time (MRT) [39, 40] collision operator. Many previous studies have reported that the MRT collision operator shows better numerical stability than the BGK collision operator [39, 41, 42]. Using the MRT collision operator, the LB equation can be written as follows [29]:

$$f_\alpha\left(\mathbf{x}+\mathbf{e}_\alpha\delta_t,\ t+\delta_t\right)=f_\alpha\left(\mathbf{x},\ t\right)-\bar{\Lambda}_{\alpha\beta}\left(f_\beta-f_\beta^{eq}\right)\Big|_{(\mathbf{x},\ t)}+\delta_t\left(G_\alpha-0.5\bar{\Lambda}_{\alpha\beta}G_\beta\right)\Big|_{(\mathbf{x},\ t)}, \tag{1}$$

where f_α is the density distribution function, f_β^{eq} is the equilibrium distribution function in the βth direction, $\mathbf{x}$ is the spatial site, $\mathbf{e}_\alpha$ is the discrete velocity, t is the time, δ_t is the time step, $\bar{\Lambda}_{\alpha\beta}$ is the collision operator given by $\bar{\Lambda}_{\alpha\beta}=\left(\mathbf{M}^{-1}\mathbf{\Lambda}\mathbf{M}\right)_{\alpha\beta}$, in which $\mathbf{M}$ is a transformation matrix and $\mathbf{\Lambda}$ is a diagonal matrix, and G_α is the forcing term in the discrete velocity space.

With the transformation matrix $\mathbf{M}$, the right-hand side of the LB equation, i.e., Eq. (1), can be mapped onto the moment space:

$$\mathbf{m}^*=\mathbf{m}-\mathbf{\Lambda}\left(\mathbf{m}-\mathbf{m}^{eq}\right)+\delta_t\left(\mathbf{I}-\frac{\mathbf{\Lambda}}{2}\right)\mathbf{S}, \tag{2}$$

where $\mathbf{m}$ and $\mathbf{m}^{eq}$ are the moments and the equilibria in the moment space, deriving from $\mathbf{m}=\mathbf{M}\mathbf{f}$ and $\mathbf{m}^{eq}=\mathbf{M}\mathbf{f}^{eq}$, respectively, $\mathbf{I}$ is the unit matrix, and $\mathbf{S}=\mathbf{M}\mathbf{G}$ is the forcing term in the moment space.

In this study, the three-dimensional nineteen-velocity (D3Q19) lattice is utilized and the corresponding lattice velocities are given by [33]

$$\mathbf{e}_\alpha=\begin{bmatrix}0&1&-1&0&0&0&0&1&-1&1&-1&1&-1&1&-1&0&0&0&0\\0&0&0&1&-1&0&0&1&-1&-1&1&0&0&0&0&1&-1&1&-1\\0&0&0&0&0&1&-1&0&0&0&0&1&-1&-1&1&1&-1&-1&1\end{bmatrix}. \tag{3}$$

The basic idea behind the MRT collision operator is to relax the moments with individual relaxation rates. Accordingly, the diagonal matrix $\mathbf{\Lambda}$ for the relaxation rates can be expressed as follows:

$$\mathbf{\Lambda}=\mathrm{diag}\left(1,\,1,\,1,\,1,\,s_e,s_v,s_v,s_v,s_v,s_v,s_q,s_q,s_q,s_q,s_q,s_\pi,s_\pi,s_\pi\right), \tag{4}$$

where s_e and s_v are determined by the bulk and shear viscosities, respectively, while s_q and s_π are free parameters related to high-order non-hydrodynamic moments. The details of the equilibria $\mathbf{m}^{eq}$ and the forcing term **S** can be found in Ref. [33].

After the collision step in the moment space, $\mathbf{m}^*$ can be transformed back to the discrete velocity space with $\mathbf{f}^* = \mathbf{M}^{-1}\mathbf{m}^*$ using an inverse matrix $\mathbf{M}^{-1}$ of the transformation matrix, and the streaming process is given by

$$f_\alpha\left(\mathbf{x}+\mathbf{e}_\alpha\delta_t,\ t+\delta_t\right) = f_\alpha^*\left(\mathbf{x},\ t\right). \tag{5}$$

Then the macroscopic density and velocity can be calculated via

$$\rho = \sum_\alpha f_\alpha, \quad \rho\mathbf{u} = \sum_\alpha \mathbf{e}_\alpha f_\alpha + \frac{\delta_t}{2}\mathbf{F}, \tag{6}$$

where **F** is the total force acting on the system, including the interaction force $\mathbf{F}_\mathrm{m}$ and the buoyancy force $\mathbf{F}_\mathrm{b}$. For a single-component multiphase system, the interaction force at site **x** can be defined as [41, 43]

$$\mathbf{F}_\mathrm{m} = -G\psi\left(\mathbf{x}\right)\sum_\alpha w_\alpha \psi\left(\mathbf{x}+\mathbf{e}_\alpha\delta_t\right)\mathbf{e}_\alpha, \tag{7}$$

where G is a parameter controlling the strength of the interaction force, $\psi\left(\mathbf{x}\right)$ is the pseudopotential, and w_α are the weights given by $w_{1-6} = 1/6$ and $w_{7-18} = 1/12$. The buoyancy force $\mathbf{F}_\mathrm{b}$ is given by $\mathbf{F}_\mathrm{b} = \left(\rho - \rho_\mathrm{ave}\right)\mathbf{g}$, in which ρ_ave is the average fluid density of the computational domain and $\mathbf{g} = \left(0,\ 0,\ -g\right)$ is the gravitational acceleration in which $g = 3\times10^{-5}$.

The pseudopotential $\psi\left(\mathbf{x}\right)$ in Eq. (7) is chosen as $\psi\left(\mathbf{x}\right) = \sqrt{2\left(p_\mathrm{EOS} - \rho c_s^2\right)/Gc^2}$ [44, 45], where $c = 1$ is the lattice speed and p_EOS is a non-ideal equation of state. In the present work, the Peng-Robinson equation of state is employed [45]

$$p_\mathrm{EOS} = \frac{\rho RT}{1-b\rho} - \frac{a\varphi\left(T\right)\rho^2}{1+2b\rho-b^2\rho^2}, \tag{8}$$

where $\varphi\left(T\right) = \left[1+\left(0.37464+1.54226\omega-0.26992\omega^2\right)\left(1-\sqrt{T/T_c}\right)\right]^2$ in which $\omega = 0.344$ is the acentric factor, $a = 0.45724R^2T_c^2/p_c$, and $b = 0.0778RT_c/p_c$ with T_c and p_c being the critical temperature and

the critical pressure, respectively. The parameters are taken as $a = 3/49$, $b = 2/21$, and $R = 1$ [41]. By neglecting the viscous heat dissipation, the temperature field of non-ideal fluids is governed by [46, 47]

$$\partial_t T + \mathbf{u}\cdot\nabla T = \frac{1}{\rho c_V}\nabla\cdot\left(\lambda\nabla T\right) - \frac{T}{\rho c_V}\left(\frac{\partial p_{\mathrm{EOS}}}{\partial T}\right)_{\rho}\nabla\cdot\mathbf{u}, \tag{9}$$

where λ is the thermal conductivity and c_V is the specific heat at constant volume. The thermal conductivity is taken as

$$\lambda = \lambda_V\frac{\rho_L-\rho}{\rho_L-\rho_V} + \lambda_L\frac{\rho-\rho_V}{\rho_L-\rho_V}, \tag{10}$$

where λ_V is defined as $\lambda_V = \rho_V c_V \chi_V$, in which χ_V is taken as 0.03. The ratio λ_L/λ_V is chosen as 15. The saturation temperature is set to $T_s = 0.8T_c$, which corresponds to the liquid density $\rho_L \approx 7.2$ and the vapor density $\rho_V \approx 0.197$. Here it is worth mentioning that the quantities in the present study are taken in the lattice units, i.e., the units of the LB method. The conversion between the lattice units and the physical units can be found in Refs. [48, 49]. To solve Eq. (9), the classical fourth-order Runge-Kutta scheme is adopted for the time discretization and the isotropic central schemes are employed for the spatial discretization. The details of these schemes can be found in Refs. [33, 41]. The thermodynamic consistency of this 3D thermal multiphase LB model and its capability for simulating liquid-vapor phase change have been validated in the appendix of Ref. [34], in which the D^2 law for vaporization was well verified.

3. Numerical results and discussion

3.1. The simulation setup

The newly conceived pillar-structured surface with distributed wettability-modified regions is sketched in Fig. 1. The domain within the red dotted lines is taken as the computational domain. The grid size corresponding to the computational domain is chosen as $L_x \times L_y \times L_z = 150\ \text{l.u.} \times 150\ \text{l.u.} \times 250\ \text{l.u.}$, where l.u. represents the lattice units. As shown in Fig. 1, four wettability-modified regions are located on the top of each pillar. The contact angles of the wettability-modified regions and other parts of the

pillar-structured surface are denoted by θ_{pho} and θ_{phi}, respectively. The distribution of the four wettability-modified regions on the pillar top is controlled by the parameters W_{m} and D_{s}, which represent the width of each wettability-modified region and the distance between the region and the edge of the pillar top, respectively. The width of the pillar is denoted by W. It can be readily verified that the four wettability-modified regions will degrade into a unified wettability-modified region when $D_{\text{s}} + W_{\text{m}} = W/2$.

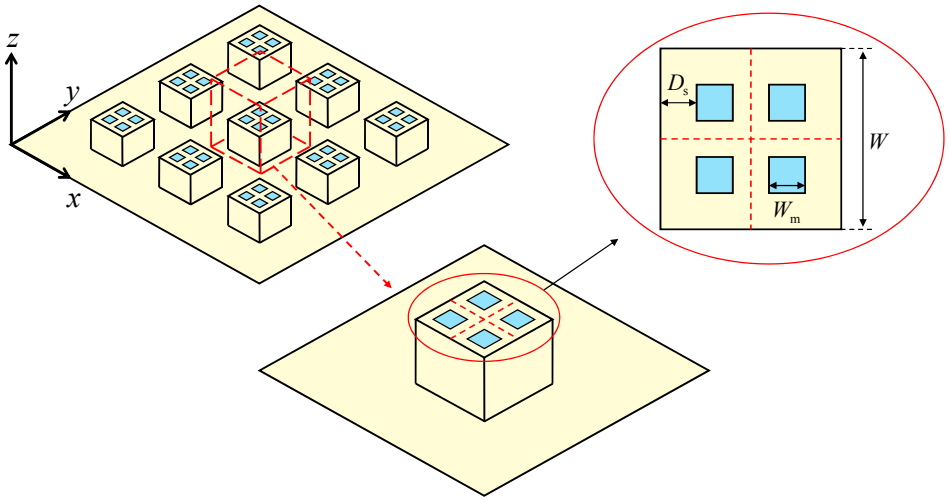

Fig. 1. Sketch of the newly conceived pillar-structured surface with distributed wettability-modified regions. The parameters W_{m} and D_{s} represent the width of each wettability-modified region (the light-blue square region) and the distance between the region and the pillar edge, respectively.

Initially, the temperature of the computational domain is taken as the saturated temperature $T_s = 0.8T_c$. Meanwhile, the temperature of the heating surface is given by $T_b = T_s + \Delta T$, in which ΔT is the wall superheat, while the temperature of the top boundary is maintained at T_s. The height of the pillar is taken as $H = 20$ l.u. and the contact angles θ_{pho} and θ_{phi} at the saturated temperature are chosen as $\theta_{\text{pho}} \approx 94^\circ$ and $\theta_{\text{phi}} \approx 37^\circ$, respectively. At $t = 0$, the computational domain is filled with a liquid phase ($0 \text{ l.u.} \le z < 150 \text{ l.u.}$) below its saturated vapor phase ($150 \text{ l.u.} \le z \le L_z$). The periodic boundary condition is implemented in the x and y directions of the computational domain and the Zou-He boundary scheme [50] is employed at the heating surface.

3.2. Boiling performance and bubble dynamics on the pillar-structured surface with distributed wettability-modified regions

In this section, the boiling performance and the bubble dynamics on the pillar-structured surface with distributed wettability-modified regions are numerically investigated. In simulations, the wall superheat is taken as $\Delta T = 0.015$, the width of the pillar is $W = 100$ l.u., and the width of each wettability-modified region is chosen as $W_{\mathrm{m}} = 20$ l.u. Figure 2(a) displays the variation of the normalized heat flux against D_{s}. Note that, the heat flux is defined as the time and spatial average of local transient heat flux during 2×10^4 time steps, and then the normalized spatial- and time-average heat flux is obtained via $\overline{h} = h\Delta x/\left(\lambda_V T_c\right)$ [34], where Δx is the grid spacing and λ_V is the thermal conductivity of vapor phase. The points A, B, C, D, and E in Fig. 2(a) represent the cases of $D_{\mathrm{s}} = 10$ l.u., 20 l.u., 23 l.u., 28 l.u., and 30 l.u., respectively.

From Fig. 2(a) we can see that the heat flux initially increases with increasing D_{s} and reaches its peak value at $D_{\mathrm{s}} = 10$ l.u. (case A), and then a relatively stable development can be observed within $10\ \text{l.u.} \le D_{\mathrm{s}} \le 15\ \text{l.u.}$ After that, the heat flux decreases with the increase of D_{s} but slightly rises from case B to case C. Finally, it declines sharply toward its lowest value at $D_{\mathrm{s}} = 30$ l.u. (case E). Note that, in case E, the four wettability-modified regions degrade into a unified wettability-modified region since in this case $D_{\mathrm{s}} + W_{\mathrm{m}} = W/2$. Clearly, the numerical results show that the boiling heat flux is increased when a unified wettability-modified region is separated into four wettability-modified regions.

To further illustrate the results displayed in Fig. 2(a), the normalized spatial- and time-average heat fluxes on the pillar top, the lateral walls of the pillar, and the bottom surface are also evaluated and depicted in Fig. 2(b). From the figure it can be seen that the heat fluxes on the lateral walls and the bottom surface change slightly with the increase of D_{s}, while the heat flux on the pillar top varies considerably and shows the same trend as the normalized spatial- and time-average heat flux of the whole heating surface in Fig. 2(a), which indicates that the variation of the heat flux on the pillar-structured surface with distributed wettability-modified regions is mainly determined by the heat flux on the pillar top, which is in turn related

to the distribution of the wettability-modified regions.

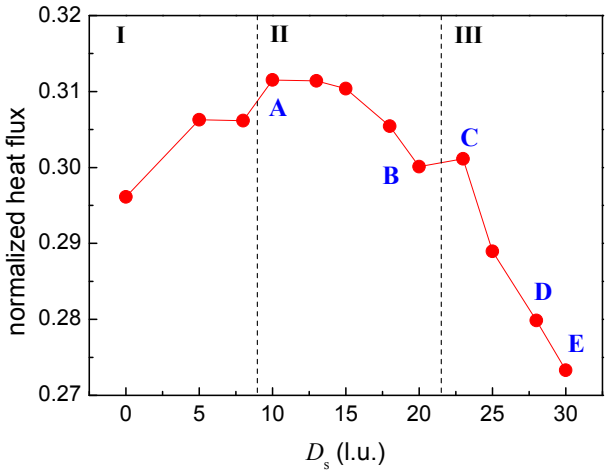

(a)

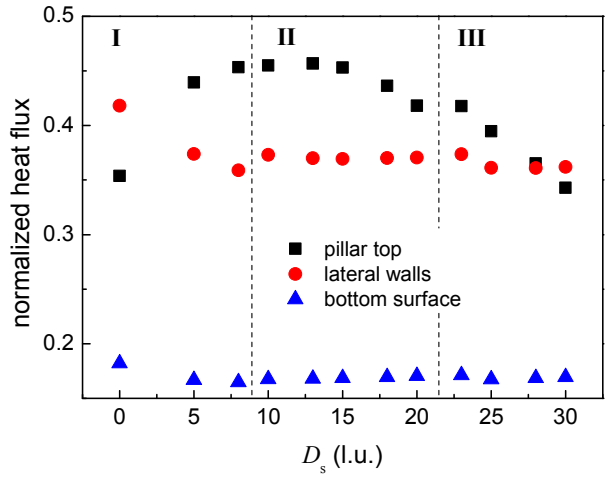

(b)

Fig. 2. Boiling performance on the pillar-structured surface with distributed wettability-modified regions. The wall superheat is taken as $\Delta T = 0.015$. (a) Variation of the normalized spatial- and time-average heat flux of the whole heating surface against D_s. The points A, B, C, D and E represent the cases of $D_s = 10$ l.u., 20 l.u., 23 l.u., 28 l.u., and 30 l.u., respectively. (b) Variations of the normalized spatial- and time-average heat fluxes on the pillar top, the lateral walls of the pillar, and the bottom surface against D_s.

The bubble dynamics during the boiling processes on the pillar-structured surface with distributed wettability-modified regions is now analyzed. Figure 3 displays some snapshots of the boiling processes in the cases of $D_s = 0$ l.u. and $D_s = 5$ l.u., respectively. From Fig. 3(a) we can see that in the case of

$D_s = 0$ l.u. the bubbles nucleated at the wettability-modified regions mainly serve as a vapor bridge to connect the adjacent bubbles generated at the bottom substrate, which leads to the bubble coalescence occurring above the pillar. The coalesced bubble covers a certain portion of the pillar and is seemingly difficult to be detached from the heating surface, which blocks the path for liquid returning. As D_s increases to 5 l.u., the bubbles on the pillar top are relatively far away from the bubbles generated at the bottom substrate and the bubble coalescence is delayed to $t \approx 8000\delta_t$, as shown in the third panel of Fig. 3(b). After that, the coalesced bubble is broken around $t \approx 10000\delta_t$, which offers paths for liquid returning. Hence, the heat flux is relatively increased in comparison with the case of $D_s = 0$ l.u., as seen in Fig. 2(a).

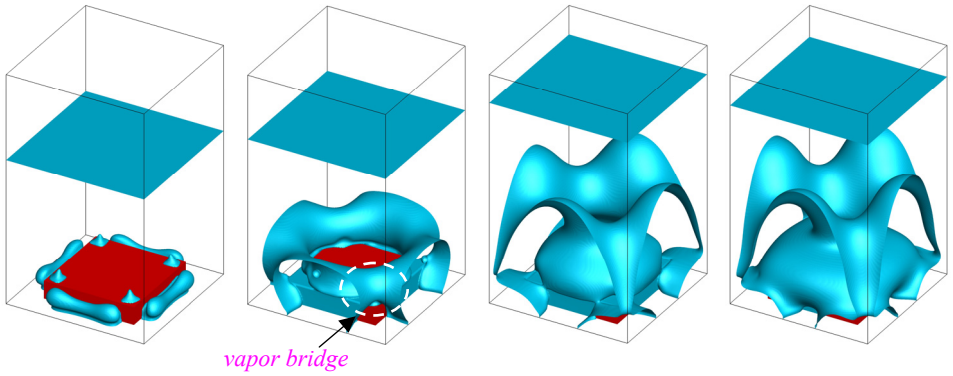

(a) $D_s = 0$ l.u.

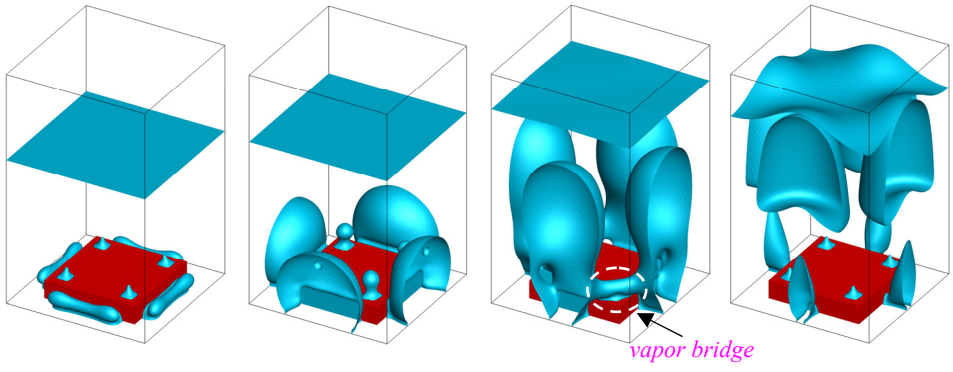

(b) $D_s = 5$ l.u.

Fig. 3. Snapshots of boiling on the pillar-structured surface with distributed wettability-modified regions in the cases of (a) $D_s = 0$ l.u. and (b) $D_s = 5$ l.u. From left to right: $t = 3000\delta_t$, $5000\delta_t$, $8000\delta_t$, and $10000\delta_t$, respectively.

Figure 4 gives the snapshots of the boiling processes in the cases of $D_s = 10$ l.u. and $D_s = 20$ l.u., respectively, which correspond to cases A and B marked in Fig. 2(a), respectively. In these two cases, the wettability-modified regions are farther away from the pillar edge in comparison with the cases presented in Fig. 3. Consequently, the bubbles on the pillar top will not coalesce with those around the pillar. Such a phenomenon is completely different from that observed in Fig. 3.

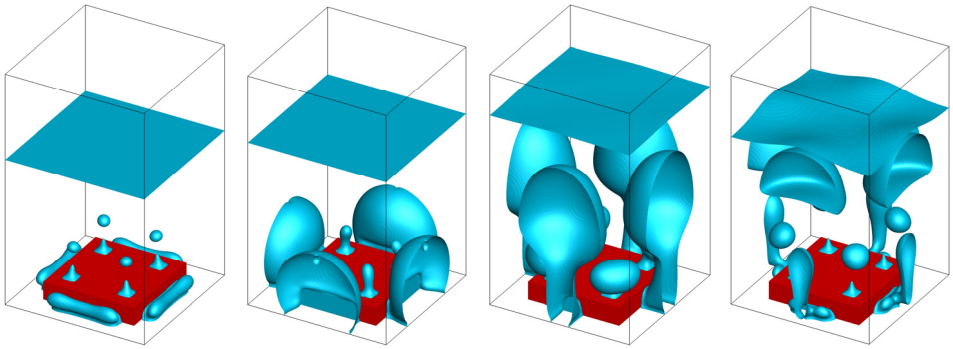

(a) $D_s = 10$ l.u.

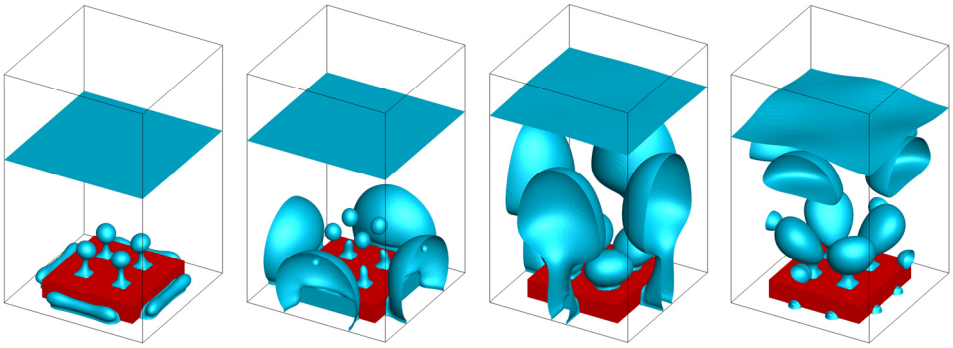

(b) $D_s = 20$ l.u.

Fig. 4. Snapshots of boiling on the pillar-structured surface with distributed wettability-modified regions in the cases of (a) $D_s = 10$ l.u. and (b) $D_s = 20$ l.u. From left to right: $t = 3000\delta_t$, $5000\delta_t$, $8000\delta_t$, and $10000\delta_t$, respectively.

Actually, according to the numerical results, the bubble dynamics on the pillar-structured surface with distributed wettability-modified regions can be classified into three regimes, namely the regimes I, II, and III labeled in Fig. 2. For the regime I, its characteristic lies in that the bubbles nucleated on the pillar top can easily coalesce with the bubbles generated at the bottom substrate since the wettability-modified

regions on the pillar top are close to the pillar edge. In contrast, the characteristic of the regime II is that the bubbles nucleated at the wettability-modified regions neither coalesce with each other nor coalesce with the bubbles nucleated at the bottom substrate. However, it should be noted that in the regime II the bubbles nucleated at the bottom substrate still affect the growth and departure of the bubbles on the pillar top, which is attributed to the *bubble-wake effect*.

When a bubble rises under the buoyancy force, it will cause the pressure of the bubble's wake region to be lower than that of other regions. As a result, the surrounding liquid will flow quickly into the wake region with an entrainment velocity, offering the so-called bubble-wake effect, which is an important effect resulting from bubble rising. Takeyama and Kunugi [51] have investigated the bubble-wake effect by applying the particle tracking visualization technology to observe the liquid flow around a single bubble. They observed that the particles around the bubble follow the bubble rising after the bubble departure. Recently, Qi *et al*. [52] experimentally reported the influences of the bubble-wake effect on the bubble dynamics during a boiling process. They found that the bubble-wake effect can shorten the bubble growth cycle and decrease the bubble departure diameter.

The bubble-wake effect can be clearly observed in the right-hand two panels of Fig. 4. By comparing the results of case A ($D_s = 10$ l.u.) with those of case B ($D_s = 20$ l.u.) at $t = 10000\delta_t$, we can see that in the former case the bubbles yielded by the wettability-modified regions have been detached from the pillar top, while in the latter case the bubbles on the pillar top still stay in the period of bubble necking. Such a difference is attributed to the fact that in case A the wettability-modified regions are much closer to the pillar edge than that in case B, which causes a stronger bubble-wake effect in case A. Correspondingly, the bubble growth cycle is shortened and the bubble departure diameter becomes smaller in case A, as seen from the right-hand panel of Fig. 4(a) and that of Fig. 4(b).

In fact, the high heat fluxes achieved in the cases of $10 \text{ l.u.} \le D_s \le 15 \text{ l.u.}$ arise from the synergistic effect of surface structure and mixed wettability. In these cases, the bubbles nucleated at the

wettability-modified regions do not coalesce with the bubbles generated at the bottom substrate, which therefore prevents the formation of a coalesced bubble covering the pillar top. Meanwhile, in these cases a relatively strong bubble-wake effect is supplied by the bubbles generated at the bottom substrate, which promotes the departure of the bubbles on the pillar top.

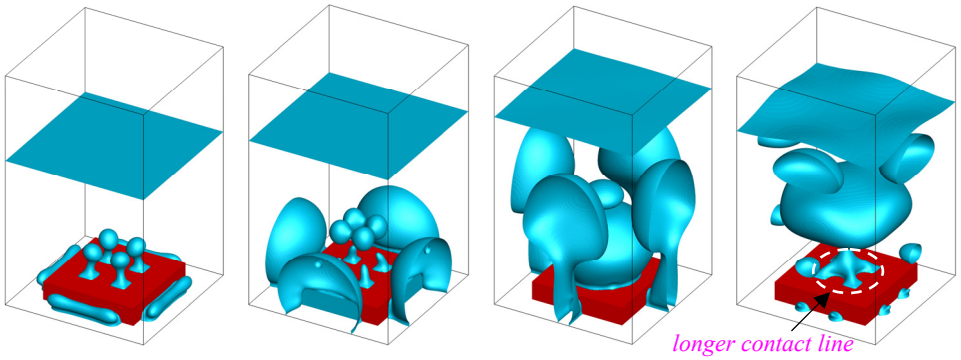

(a) $D_s = 23$ l.u.

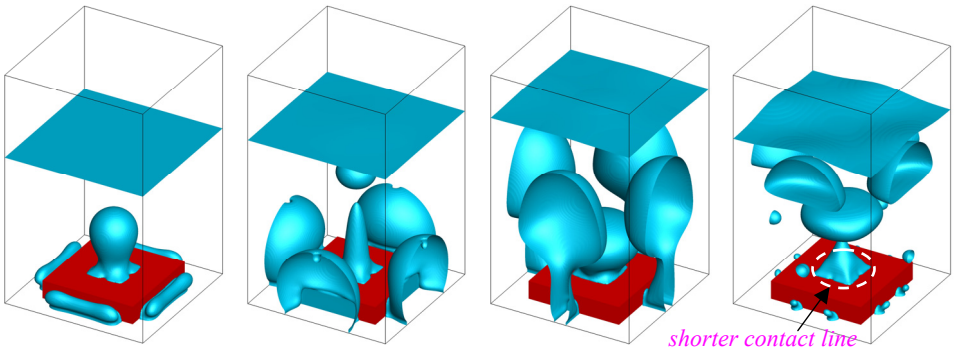

(b) $D_s = 28$ l.u.

Fig. 5. Snapshots of boiling on the pillar-structured surface with distributed wettability-modified regions in the cases of (a) $D_s = 23$ l.u. and (b) $D_s = 28$ l.u. From left to right: $t = 3000\delta_t$, $5000\delta_t$, $8000\delta_t$, and $10000\delta_t$, respectively.

Figure 5 displays some snapshots of the boiling processes on the pillar-structured surface with distributed wettability-modified regions in the cases of $D_s = 23$ l.u. and $D_s = 28$ l.u., respectively, which fall into the regime III labeled in Fig. 2. In the case of $D_s = 23$ l.u., we can see that, at $t = 3000\delta_t$, the bubbles nucleated at the wettability-modified regions grow obliquely owing to the mutual attraction

between the growing bubbles. Such an attraction phenomenon of bubbles can also be found in Ref. [53]. Subsequently, as seen in the second panel ($t = 5000\delta_t$) of Fig. 5(a), each bubble on the pillar top is separated into two parts, i.e., a detached bubble and a residual bubble. Later, the detached bubbles coalesce with each other during the rising process. Meanwhile, the four residual bubble act as the nuclei of the next boiling cycle and quickly grow. In the next boiling cycle, the four bubbles on the pillar top coalesce with each other and expand vigorously. With the expansion of the coalesced bubble on the pillar top, the hydrophilic region between the hydrophobic wettability-modified regions is also covered by the vapor phase. Nevertheless, during the bubble necking process from $t = 8000\delta_t$ to $10000\delta_t$, some parts of the covered hydrophilic region are exposed again to the fresh liquid (see the right-hand panel of Fig. 5(a)).

When D_s increases to 28 l.u., the bubble dynamics on the pillar-structured surface with distributed wettability-modified regions is similar to that on the pillar-structured surface with a unified wettability-modified region ($D_s = 30$ l.u.). As shown in Fig. 5(b), the bubbles nucleated at the wettability-modified regions are so close that the bubble coalescence occurs very early during the boiling process. The coalesced bubble is later separated into a detached bubble and a residual bubble. The hydrophilic region between the hydrophobic wettability-modified regions is continuously covered by vapor. Moreover, we can observe that the triple-phase contact line on the pillar top in the case of $D_s = 28$ l.u. is much shorter than that in the case of $D_s = 23$ l.u., as shown in the right-hand panel of Fig. 5, which may be one of the reasons why the heat flux declines in the regime III.

As observed in Fig. 5, the main characteristic of the regime III is that the bubbles generated on the pillar top coalesce with each other because the wettability-modified regions are too far away from the pillar edge but very close to each other. The bubble coalescence occurring on the pillar top causes the hydrophilic region between the hydrophobic wettability-modified regions to be covered by the residual vapor. Hence, the boiling in the regime III with $20 \text{ l.u.} < D_s \leq 30 \text{ l.u.}$ exhibits a relatively low heat flux.

3.3. Analyses of dry spots and triple-phase contact lines for revealing the associated mechanism

To further reveal the boiling mechanism on the pillar-structured surface with distributed wettability-modified regions, the dry spots and the triple-phase contact lines on the pillar top during the boiling processes of different cases are analyzed in this section. Firstly, a comparative analysis is made between case A ($D_s = 10$ l.u.) and case E ($D_s = 30$ l.u.). Note that case E represents the case of the pillar-structured surface with a unified wettability region. Figures 6 and 7 illustrate the boiling characteristics of cases A and E from $t = 7000\delta_t$ to $11000\delta_t$, respectively, in which the bubble expansion, bubble necking, and bubble departure are displayed. Particularly, the corresponding temperature contours of the *x*-*y* cross section at $z = H + 1$ are also shown in these figures.

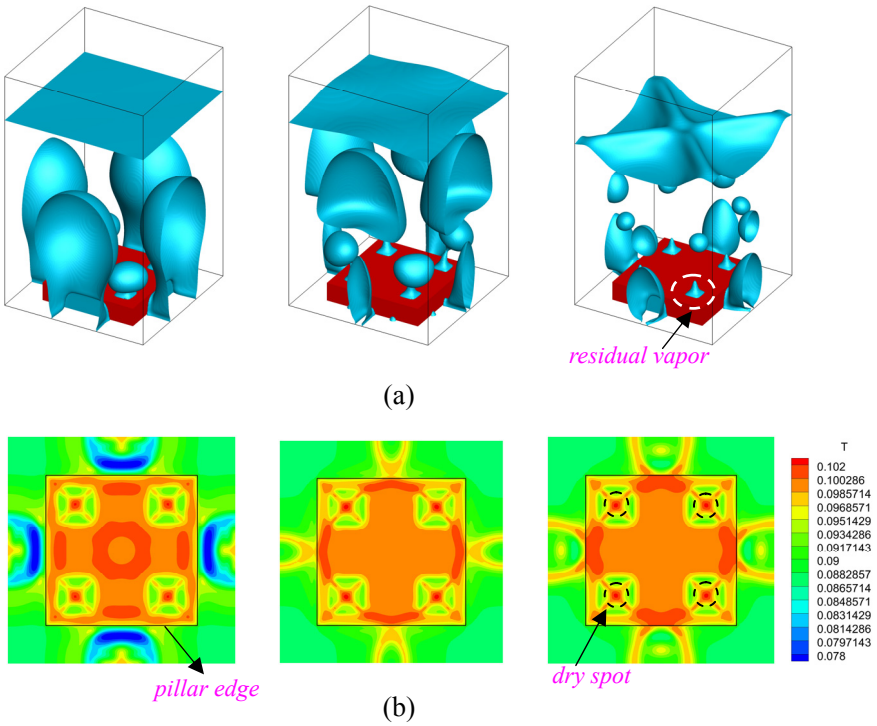

Fig. 6. Boiling characteristics of case A ($D_s = 10$ l.u.). (a) bubble dynamics and (b) temperature contours of the *x*-*y* cross section at $z = H + 1$. From left to right: $t = 7000\delta_t$, $9000\delta_t$, and $11000\delta_t$, respectively.

By comparing Fig. 6(a) with Fig. 7(a), a similar bubble behavior can be observed for cases A and E. On the pillar top, at $t = 7000\delta_t$, the residual vapor bubbles resulting from the last boiling cycle are growing at the hydrophobic wettability-modified regions. Subsequently, the bubbles begin to depart as the

bubble neck shrinks, which can be seen in the second panels of Fig. 6(a) and Fig. 7(a). Later, each bubble is separated into a detached bubble and a residual bubble, which remains on the pillar top and serves as a bubble nucleation site for the next boiling cycle. During this process, it can be observed that the wettability-modified regions are covered by the vapor phase, which leads to the formation of hot dry spots underneath the bubbles.

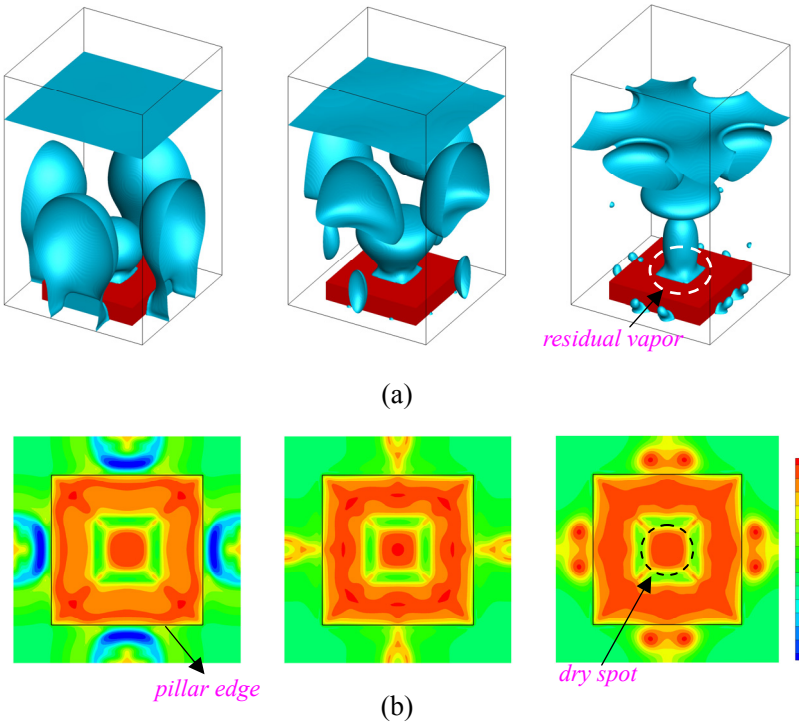

Fig. 7. Boiling characteristics of case E ($D_s = 30$ l.u.). (a) bubble dynamics and (b) temperature contours of the *x*-*y* cross section at $z = H + 1$. From left to right: $t = 7000\delta_t$, $9000\delta_t$, and $11000\delta_t$, respectively.

Figures 6(b) and 7(b) depict the temperature contours of the *x*-*y* cross section at $z = H + 1$ of cases A and E, respectively. From these figures a high fluid temperature can be observed at the hydrophobic wettability-modified regions that are covered by vapor bubbles, which also confirms the formation of hot dry spots underneath the bubbles on the pillar top. Besides, the hydrophilic region of the pillar top also shows a relatively high fluid temperature. This is because the convection heat transfer occurs at the hydrophilic region without phase change. Conversely, the regions of triple-phase contact lines on the pillar top show a much lower fluid temperature, which indicates that the liquid-vapor phase change occurs at

these regions is very strong. Accordingly, these regions will offer a high heat flux.

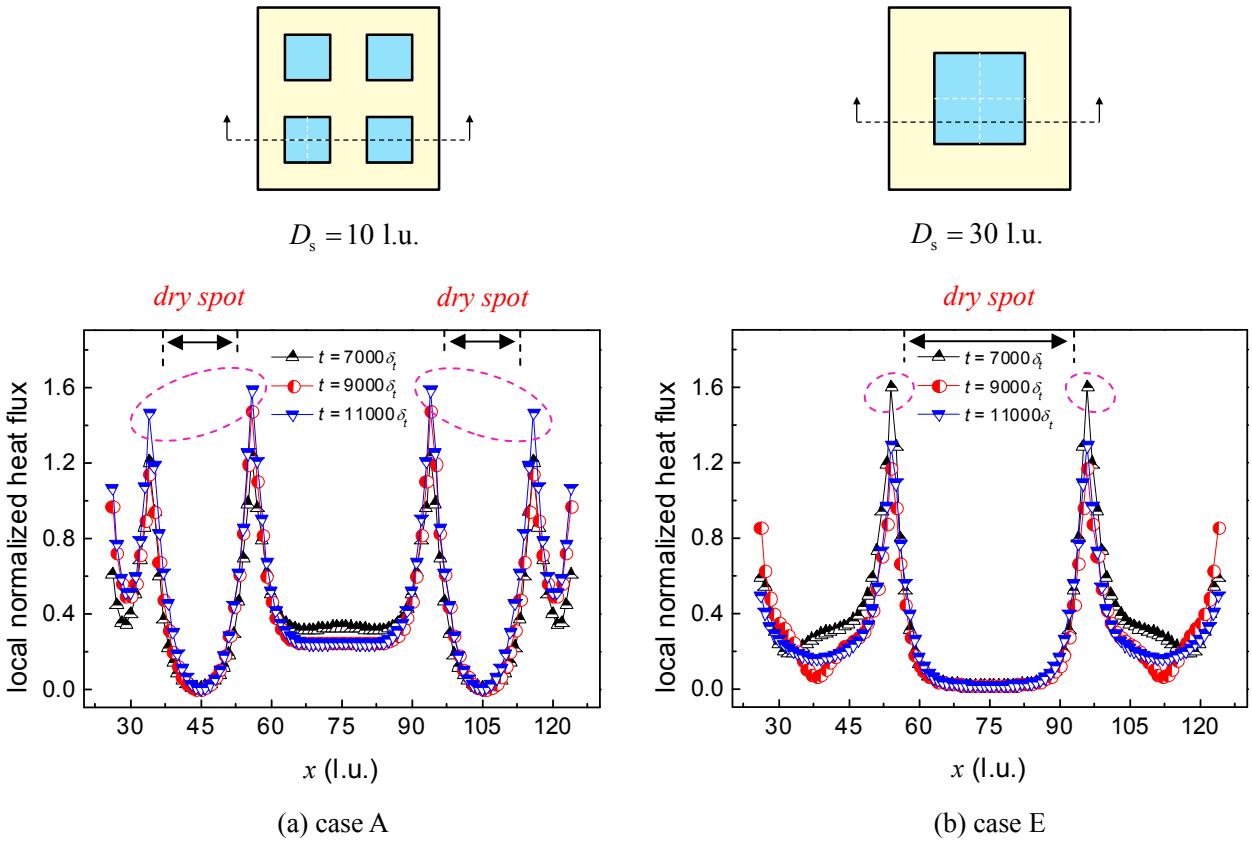

(a) case A (b) case E

Fig. 8. The profiles of local normalized heat fluxes on the pillar top at $t = 7000\delta_t$, $9000\delta_t$, and $11000\delta_t$ along the black dotted lines plotted in the top panel of this figure. (a) case A and (b) case E. It can be found that the peaks appear at the regions of triple-phase contact lines.

To illustrate the aforementioned point more clearly, the profiles of local transient normalized heat fluxes on the pillar top at $t = 7000\delta_t$, $9000\delta_t$, and $11000\delta_t$ are displayed in Figs. 8(a) and 8(b) for the cases A and E, respectively. The heat fluxes are calculated along the black dotted lines plotted in the top panel of Fig. 8. The figure clearly shows that on the pillar top the lowest heat flux occurs at the central regions of dry spots, while the highest heat flux is achieved at the regions of triple-phase contact lines. Moreover, from Fig. 8 we can also observe that there are four peaks in case A but only two peaks in case E, which is attributed to the fact that the length of the triple-phase contact lines on the pillar top in case A is generally two times as long as that in case E. This is also one of the reasons why the pillar-structured

surface with distributed wettability-modified regions exhibits better boiling performance than that with a unified wettability-modified region.

Now we turn our attention to comparing case A ($D_s = 10$ l.u.) with case B ($D_s = 20$ l.u.) by analyzing the dry spot area ratio and the transient heat flux on the pillar top. The dry spot area represents the area of dry spots caused by the bubbles nucleated on the pillar top and then the dry spot area ratio is defined as the ratio of the dry spot area to the area of the whole heating surface. Figure 9 displays the variations of the dry spot area ratio and the normalized transient heat flux on the pillar top during the boiling processes of cases A and B. From Fig. 9(a) we can see that there are no significant differences between the dry spot area ratios of the two cases when $t \le 7000\delta_t$. However, after that, a sharp rise can be observed in the results of case B and the highest dry spot area ratio of case B appears at $t = 8400\delta_t$, which corresponds to the largest expansion of the bubbles on the pillar top before the bubble necking, as seen in the snapshot presented in Fig. 9(a). Accordingly, a very low transient heat flux can be observed in Fig. 9(b) at $t = 8400\delta_t$ for case B.

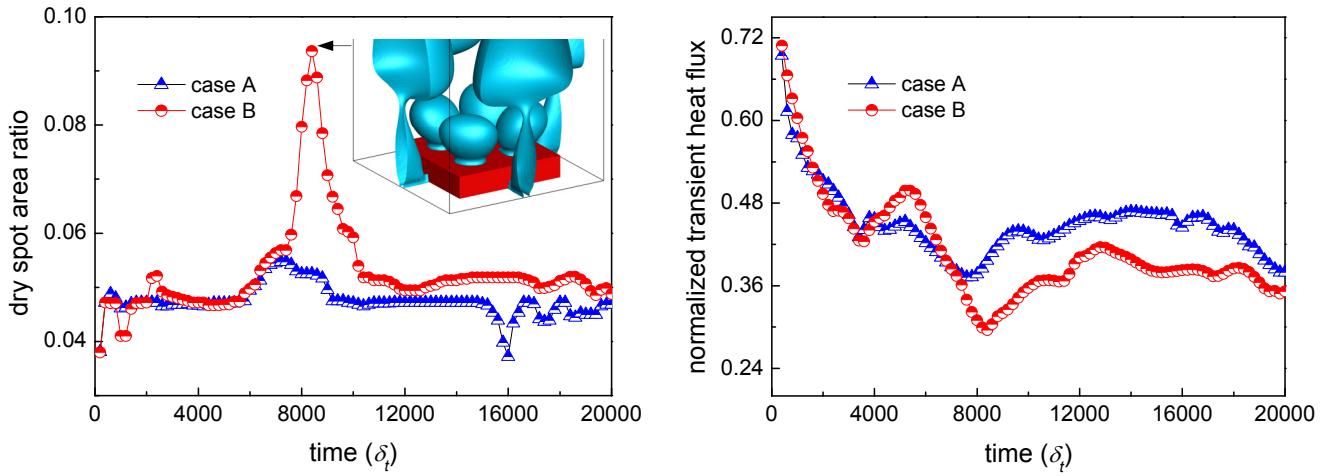

Fig. 9. Variations of (a) the dry spot area ratio and (b) the normalized transient heat flux on the pillar top during the boiling processes of cases A and B. The snapshot shown in the left panel of this figure was taken at $t = 8400\delta_t$ for case B, which corresponds to the largest dry spot area ratio on the pillar top.

In contrast, no sharp rise occurs after $t = 7000\delta_t$ in Fig. 9(a) for case A. Such a difference between cases A and B is mainly caused by the previously mentioned bubble-wake effect. In case A the wettability-modified regions are much closer to the pillar edge than that in case B. Therefore, after the departure of the bubbles nucleated at the bottom substrate, the bubbles on the pillar top in case A will receive a stronger bubble-wake effect that accelerates the bubble departure process and suppresses the bubble expansion on the pillar top. As seen in Fig. 9(a), after $t = 7000\delta_t$, the dry spot area ratio of case A is much smaller than that of case B, which is an important reason why the transient heat flux on the pillar top of case A is higher than that of case B after $t = 7000\delta_t$ (see Fig. 9(b)).

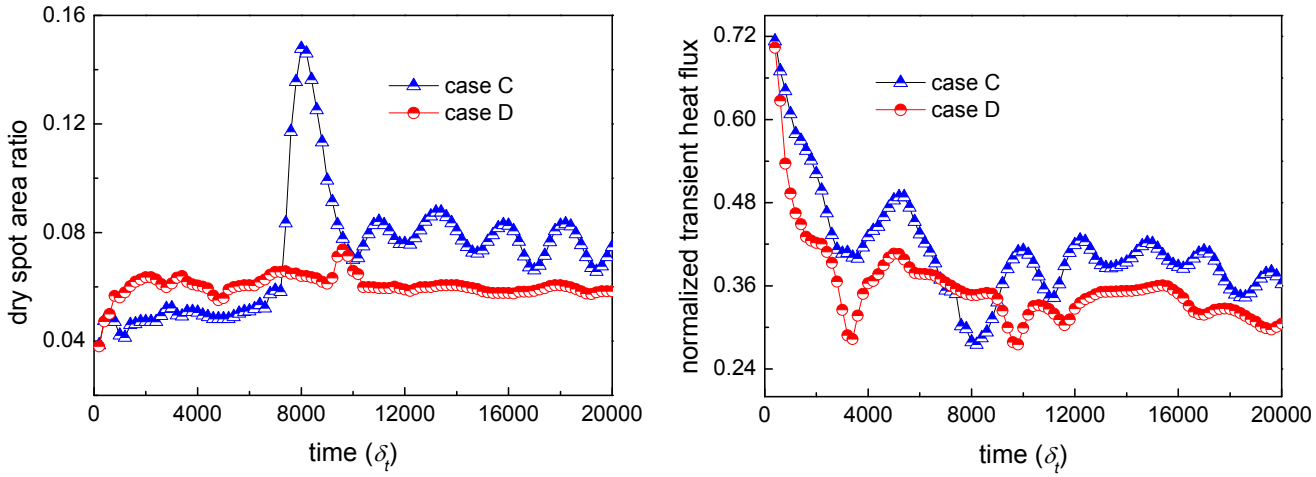

(a) (b)

Fig. 10. Variations of (a) the dry spot area ratio and (b) the normalized transient heat flux on the pillar top during the boiling processes of case C ($D_s = 23$ l.u.) and case D ($D_s = 28$ l.u.).

Finally, a comparative analysis is conducted between cases C and D. Figure 10 illustrates the variations of the dry spot area ratio and the normalized transient heat flux on the pillar top during the boiling processes of cases C and D. From Fig. 10(a) we can see that the dry spot area ratio of case C increases slowly before $t = 7000\delta_t$. After that, it increases dramatically and reaches a peak value at $t = 8000\delta_t$. Such a rise stems from the coalescence of the four bubbles on the wettability-modified regions,

which causes the hydrophilic region between the wettability-modified regions to be quickly covered by the vapor phase (see the third panel of Fig. 5(a)). After $t = 8000\delta_t$, a large portion of the covered hydrophilic region is exposed again to the fresh liquid and the dry spot area ratio decreases rapidly. Besides, we can see that the dry spot area ratio of case C fluctuates largely after $t = 10000\delta_t$, which is caused by the frequent bubble expansion and bubble necking processes. For case D, from Fig. 10(a) we can observe a rise of the dry spot area ratio before $t = 1000\delta_t$, which mainly arises from the very early bubble coalescence in this case. After that, there are no significant variations of the dry spot area ratio in case D except for the variation around $t \approx 9500\delta_t$.

Moreover, from Fig. 10(a) it can be seen that before $t = 7000\delta_t$ the dry spot area ratio of case D is larger than that of case C. Correspondingly, the transient heat flux on the pillar top of case D is lower than that of case C before $t = 7000\delta_t$, as shown in Fig. 10(b). However, after $t = 10000\delta_t$, the dry spot area ratio of case D is smaller than that of case C, but the heat flux on the pillar top of case D is still lower than that of case C. What happened? Actually, this is because the length of the triple-phase contact lines of case C is much longer than that of case D after $t = 10000\delta_t$, as shown in Fig. 11, in which the normalized length of triple-phase contact lines is defined as l_{top}/L_0, where l_{top} is the length of the triple-phase contact lines on the pillar top (does not include the triple-phase contact lines caused by the bubbles nucleated at the bottom substrate) and L_0 denotes the length of the hydrophilic-hydrophobic boundaries of the pillar-structured surface with distributed wettability-modified regions. Quantitatively, during $10000\delta_t \le t \le 20000\delta_t$, the average value of the normalized length of triple-phase contact lines in case C is about 0.894, while in case D the average value is about 0.632. Owing to such an important difference, the transient heat flux on the pillar top of case D is lower than that of case C after $t = 10000\delta_t$. When D_s is further increased to 30 l.u. (case E), the average value of the normalized length of triple-phase contact lines will be reduced to about 0.5 and then the heat flux will be further reduced.

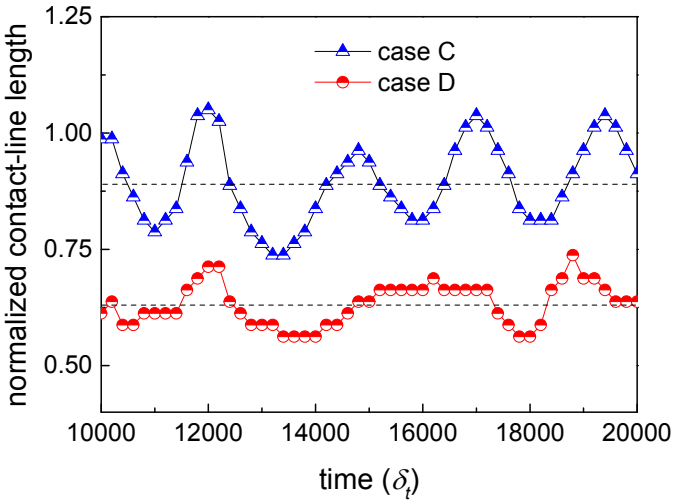

Fig. 11. Comparison of the normalized length of triple-phase contact lines on the pillar top between cases C and D during $10000\delta_t \le t \le 20000\delta_t$.

3.4. Effects of the width of wettability-modified regions and the pillar width

In this subsection, the influences of the pillar width (W) and the width of wettability-modified regions (W_m) on the boiling performance of the pillar-structured surface with distributed wettability-modified regions are investigated. Firstly, the effects of W_m in Fig. 1 are studied with the pillar width being fixed at $W = 90$ l.u. Three choices are considered for W_m, namely $W_m = 15$ l.u., 20 l.u., and 35 l.u., respectively. Figure 12 displays the variations of the normalized heat fluxes against D_s in the cases of $W_m = 15$ l.u., 20 l.u., and 35 l.u., respectively. From the figure we can see that the heat fluxes in the cases of $W_m = 15$ l.u. and 20 l.u. show the same trend and can be classified into three regimes as that exhibited in Fig. 2(a). From Fig. 12 it is clearly seen that the cases in the regime II as well as several cases that are very close to the regime II perform much better than other cases. Moreover, it can be found that the heat fluxes in the regime II increases when W_m is increased from 15 l.u. to 20 l.u., but the corresponding range of the regime II is decreased. As W_m is further increased to 35 l.u, the heat flux decreases compared with the case of $W_m = 20$ l.u. in the regime II. Particularly, in the case of $W_m = 35$ l.u. the heat flux curve cannot be classified into three regimes, as shown in Fig. 12. The main reason may be that the width

of the wettability-modified regions on the pillar top is so large that the bubbles on the pillar top not only coalesce with each other but also coalesce with the bubbles around the pillar.

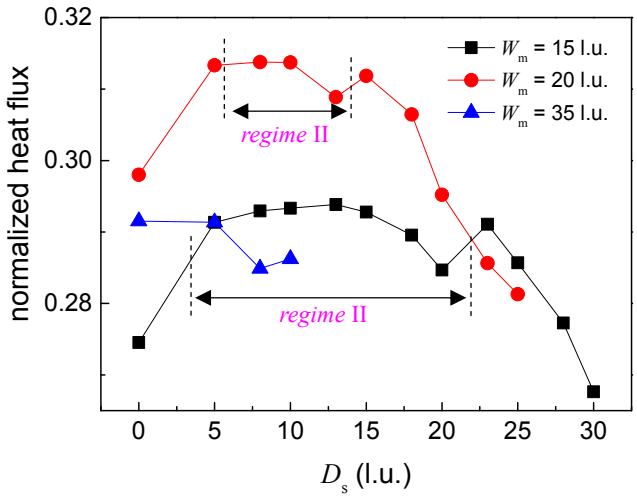

Fig. 12. Variations of the normalized heat flux on the pillar-structured surface with distributed wettability-modified regions against D_s in the cases of $W_m = 15$ l.u., 20 l.u., and 35 l.u., respectively. The pillar width is $W = 90$ l.u. and the wall superheat is taken as $\Delta T = 0.015$.

For the case of $W_m = 45$ l.u., the pillar-structured surface with distributed wettability-modified regions degrades into a pillar-structured surface in which the pillar top is completely hydrophobic. Compared with the heat flux of such a hydrophilic-hydrophobic pillar-structured surface at $\Delta T = 0.015$, the maximum heat fluxes in the cases of $W_m = 15$ l.u., 20 l.u., and 35 l.u. shown in Fig. 12 are increased by 31.26%, 40.17%, and 30.21%, respectively. Figure 13 gives some snapshots of the boiling processes on the pillar-structured surface with distributed wettability-modified regions corresponding to the two peak values in Fig. 12, i.e., the cases of $W_m = 15$ l.u. & $D_s = 13$ l.u. and $W_m = 20$ l.u. & $D_s = 8$ l.u. From Fig. 13 we can see that these two cases show a similar bubble behavior and their bubble dynamics falls into the regime II, which has been extensively discussed in the previous sections. Besides, compared with the bubbles on the pillar top in the case of $W_m = 15$ l.u., the bubbles in the case of $W_m = 20$ l.u. are much bigger because of a larger area of wettability-modified regions, which causes more intense liquid agitation.

Moreover, it can be observed that the triple-phase contact lines on the pillar top in the case of $W_m = 20$ l.u. are longer, which offer more regions for the liquid-vapor phase change. Hence its heat flux is higher than that of the case of $W_m = 15$ l.u.

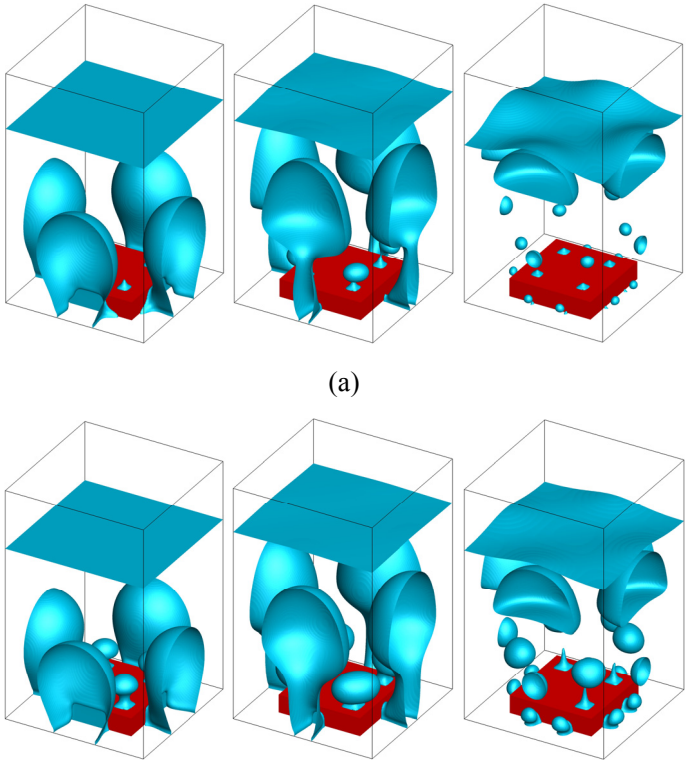

(a)

(b)

Fig. 13. Snapshots of boiling on the pillar-structured surface with distributed wettability-modified regions in the cases of (a) $W_m = 15$ l.u. & $D_s = 13$ l.u. and (b) $W_m = 20$ l.u. & $D_s = 8$ l.u. From left to right: $t = 6000\delta_t$, $8000\delta_t$, and $10000\delta_t$, respectively.

However, when W_m is further increased, the bubble coalescence may occur. Some snapshots of the boiling process in the case of $W_m = 35$ l.u. & $D_s = 5$ l.u. are shown in Fig. 14. It is obvious that, owing to a larger area of the wettability-modified regions, the bubbles on the pillar top expand rapidly to coalesce with each other at $t = 3000\delta_t$ and then further coalesce with the bubbles around the square pillar at $t = 5000\delta_t$, which causes a large portion of the heating surface to be covered by the vapor phase and prevent the fresh liquid from rewetting the heat surface. Accordingly, the heat flux is reduced.

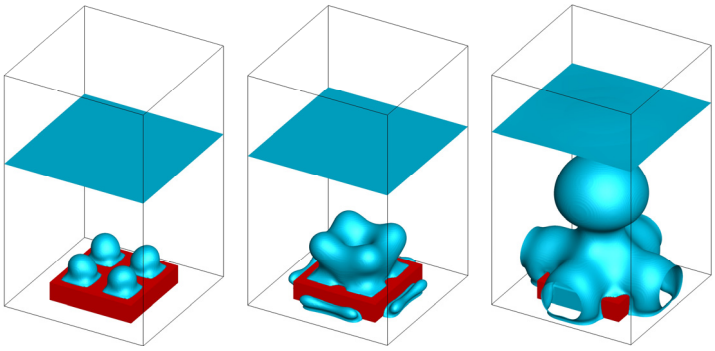

Fig. 14. Snapshots of boiling on the pillar-structured surface with distributed wettability-modified regions in the case of $W_m = 35$ l.u. & $D_s = 5$ l.u. From left to right: $t = 1000\delta_t$, $3000\delta_t$, and $5000\delta_t$, respectively.

The influences of the pillar width (W) are now investigated. The width of the wettability-modified regions is fixed at $W_m = 20$ l.u. Figure 15 illustrates the variations of the normalized heat flux on the pillar-structured surface with distributed wettability-modified regions against D_s in the cases of $W = 60$ l.u., 90 l.u., and 110 l.u., respectively. From the figure it can be seen that the heat flux in the case of $W = 60$ l.u. remains at a low level when increasing D_s and the heat flux curve in this case cannot be classified into three regimes. However, the heat flux curves in the cases of $W = 90$ l.u. and 110 l.u. can be classified into three regimes with relatively higher heat fluxes in the regime II. For these two cases, the major difference lies in that, although the case of $W = 90$ l.u. provides a narrower range of the regime II, the heat fluxes in the regime II of this case are higher than those in the case of $W = 110$ l.u.

Figure 16 gives some snapshots of the boiling process in the case of $W = 60$ l.u. & $D_s = 5$ l.u. From the figure it can be seen that the bubbles on the pillar top coalesce with each other as well as the bubbles around the pillar. Such a bubble behavior is similar to that displayed in Fig. 14, which exhibits poor boiling performance as previously discussed. Figure 17 displays some snapshots of the boiling processes on the pillar-structured surface with distributed wettability-modified regions corresponding to the two peak values in Fig. 15, i.e., the cases of $W = 90$ l.u. & $D_s = 8$ l.u. and $W = 110$ l.u. & $D_s = 18$ l.u. By comparing Fig. 17(a) with Fig. 17(b), we can see that, as the pillar width increases from $W = 90$ l.u. to

110 l.u., the bubbles nucleated at the bottom substrate expand along the lateral walls owing to the narrow distance between the adjacent pillars, which causes more regions to be covered the vapor phase, as seen from the first and second panels of Fig. 17(b). As a result, in the regime II the heat flux in the case of $W = 110$ l.u. shows a relatively lower value in comparison with that in the case of $W = 90$ l.u. In addition, when the pillar width is further increased, the space between the adjacent pillars will be very crowded and the film boiling may be triggered on the lateral walls and the bottom surface.

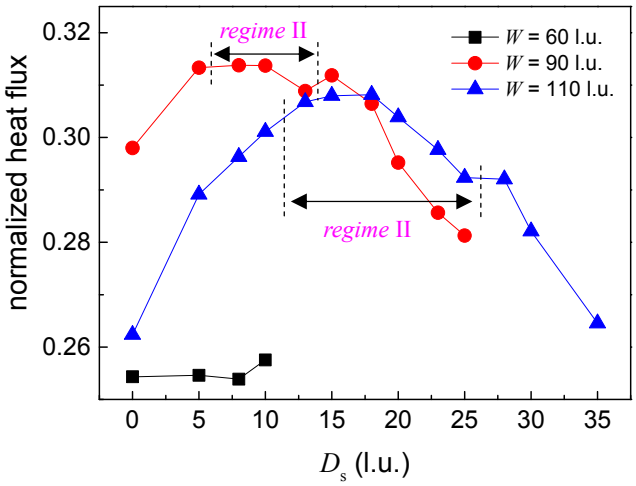

Fig. 15. Variations of the normalized heat flux on the pillar-structured surface with distributed wettability-modified regions against D_s in the cases of $W = 60$ l.u., 90 l.u., and 110 l.u. The width of the wettability-modified regions is fixed at $W_m = 20$ l.u.

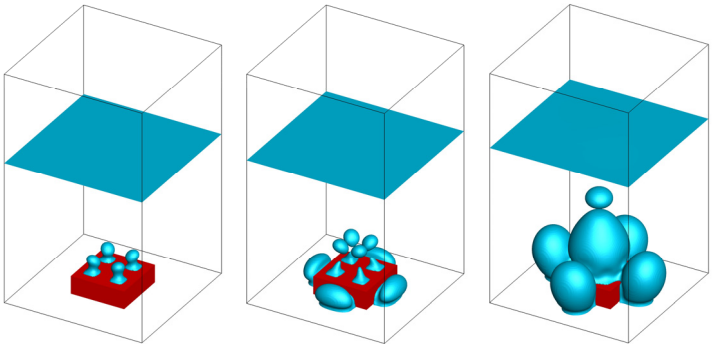

Fig. 16. Snapshots of boiling on the pillar-structured surface with distributed wettability-modified regions in the case of $W = 60$ l.u. & $D_s = 5$ l.u. From left to right: $t = 1000\delta_t$, $3000\delta_t$, and $5000\delta_t$, respectively.

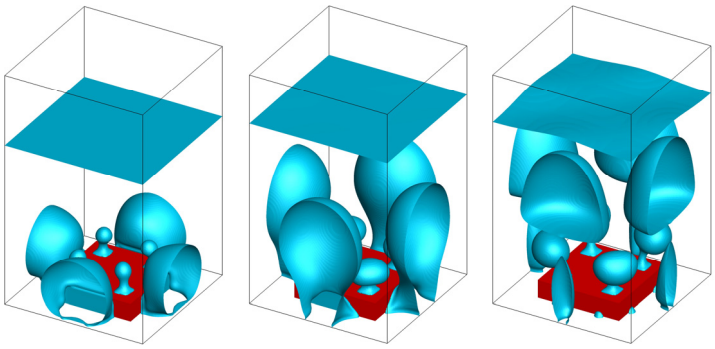

(a)

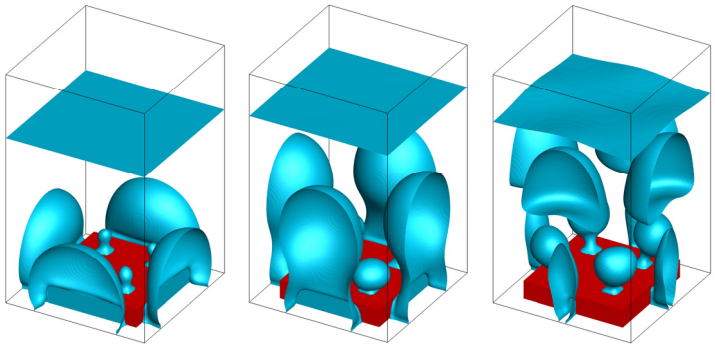

(b)

Fig. 17. Snapshots of boiling on the pillar-structured surface with distributed wettability-modified regions in the cases of (a) $W = 90$ l.u. & $D_s = 8$ l.u. and (b) $W = 110$ l.u. & $D_s = 18$ l.u. From left to right: $t = 5000\delta_t$, $7000\delta_t$, and $9000\delta_t$, respectively.

4. Conclusions

In this paper, we have conceived a novel pillar-structured surface with distributed wettability-modified regions on the top of each pillar. The boiling heat transfer performance and the bubble dynamics on the pillar-structured surface with distributed wettability-modified regions as well as the associated enhancement mechanism have been investigated by a 3D thermal multiphase LB model with liquid-vapor phase change. The main findings and conclusions are summarized as follows:

(i) By separating a unified wettability-modified region on the pillar top into four wettability-modified regions, the pillar-structured surface with distributed wettability-modified regions elongates the length of the triple-phase contact lines and therefore performs better than the pillar-structured surface with a unified wettability-modified region.

(ii) According to the distribution of the wettability-modified regions, the bubble dynamics on the newly conceived pillar-structured surface can be classified into three regimes, i.e., regimes I, II, and III, among which the regime II shows better boiling performance than the other two regimes owing to the synergistic effects of surface structure and mixed wettability.

(iii) The characteristic of the regime II lies in that in this regime the bubbles nucleated at the wettability-modified regions neither coalesce with each other nor coalesce with the bubbles nucleated at the bottom substrate. However, the bubbles on the pillar top receive a strong bubble-wake effect supplied by the bubbles generated at the bottom substrate, which shortens the bubble growth cycle and promotes the departure of the bubbles on the pillar top, and also reduces the area of dry spots on the pillar top.

(iv) The effects of the pillar width and the width of the wettability-modified regions have also been investigated. The numerical results show that the best boiling performance is always achieved in the cases that fall into the regime II.

Acknowledgments

This work was supported by the National Natural Science Foundation of China (Grant No. 51822606).

References

[1] M.-H. Chun, M.-G. Kang, Effects of Heat Exchanger Tube Parameters on Nucleate Pool Boiling Heat Transfer, Journal of Heat Transfer, 120(2) (1998) 468-476.

[2] M.J. McNelly, H.W. Huntley, E.L. Burley, Chemical engineering aspect of boiling water reactors, ; General Electric Co., San Jose, CA (United States), 1965.

[3] T. Bohdal, W. Kuczyński, Investigation of Boiling of Refrigeration Medium Under Periodic Disturbance Conditions, Experimental Heat Transfer, 18(3) (2005) 135-151.

[4] X. Chen, H. Ye, X. Fan, T. Ren, G. Zhang, A review of small heat pipes for electronics, Applied Thermal Engineering, 96 (2016) 1-17.

[5] H.M. Kurihara, J.E. Myers, The effects of superheat and surface roughness on boiling coefficients, AIChE Journal, 6(1) (1960) 83-91.

[6] S.K. Roy Chowdhury, R.H.S. Winterton, Surface effects in pool boiling, International Journal of Heat and Mass Transfer, 28(10) (1985) 1881-1889.

[7] H.S. Ahn, H. Kim, H. Jo, S. Kang, W. Chang, M.H. Kim, Experimental study of critical heat flux enhancement during forced convective flow boiling of nanofluid on a short heated surface, International Journal of Multiphase Flow, 36(5) (2010) 375-384.

[8] S. Kim, H.D. Kim, H. Kim, H.S. Ahn, H. Jo, J. Kim, M.H. Kim, Effects of nano-fluid and surfaces with nano structure on the increase of CHF, Experimental Thermal and Fluid Science, 34(4) (2010) 487-495.

[9] H. Jo, S. Kim, H. Kim, J. Kim, M.H. Kim, Nucleate boiling performance on nano/microstructures with different wetting surfaces, Nanoscale Research Letters, 7(1) (2012) 242.

[10] H. Jo, H.S. Ahn, S. Kang, M.H. Kim, A study of nucleate boiling heat transfer on hydrophilic, hydrophobic and heterogeneous wetting surfaces, International Journal of Heat and Mass Transfer, 54(25-26) (2011) 5643-5652.

[11] Y. Nam, J. Wu, G. Warrier, Y.S. Ju, Experimental and Numerical Study of Single Bubble Dynamics on a Hydrophobic Surface, Journal of Heat Transfer, 131(12) (2009).

[12] S.H. Kim, G.C. Lee, J.Y. Kang, K. Moriyama, H.S. Park, M.H. Kim, The role of surface energy in heterogeneous bubble growth on ideal surface, Int. J. Heat Mass Transf., 108 (2017) 1901-1909.

[13] Y. Takata, S. Hidaka, M. Masuda, T. Ito, Pool boiling on a superhydrophilic surface, International Journal of Energy Research, 27(2) (2003) 111-119.

[14] C.P. Costello, W.J. Frea, The roles of capillary wicking and surface deposits in the attainment of high pool boiling burnout heat fluxes, AIChE Journal, 10(3) (1964) 393-398.

[15] A.R. Betz, J. Xu, H. Qiu, D. Attinger, Do surfaces with mixed hydrophilic and hydrophobic areas enhance pool boiling?, Applied Physics Letters, 97(14) (2010).

[16] A.R. Motezakker, A.K. Sadaghiani, S. Çelik, T. Larsen, L.G. Villanueva, A. Koşar, Optimum ratio of hydrophobic to hydrophilic areas of biphilic surfaces in thermal fluid systems involving boiling, International Journal of Heat and Mass Transfer, 135 (2019) 164-174.

[17] M. Dadhich, O.S. Prajapati, A brief review on factors affecting flow and pool boiling, Renewable and Sustainable Energy Reviews, 112 (2019) 607-625.

[18] J. Kim, S. Jun, R. Laksnarain, S.M. You, Effect of surface roughness on pool boiling heat transfer at a heated surface having moderate wettability, International Journal of Heat and Mass Transfer, 101 (2016) 992-1002.

[19] C.K. Yu, D.C. Lu, T.C. Cheng, Pool boiling heat transfer on artificial micro-cavity surfaces in dielectric fluid FC-72, Journal of Micromechanics and Microengineering, 16(10) (2006) 2092-2099.

[20] H. Jo, D.I. Yu, H. Noh, H.S. Park, M.H. Kim, Boiling on spatially controlled heterogeneous surfaces: Wettability patterns on microstructures, Applied Physics Letters, 106(18) (2015).

[21] C. Shen, C. Zhang, Y. Bao, X. Wang, Y. Liu, L. Ren, Experimental investigation on enhancement of nucleate pool boiling heat transfer using hybrid wetting pillar surface at low heat fluxes, International Journal of Thermal Sciences, 130 (2018) 47–58.

[22] W. Zhang, Y. Chai, J. Xu, G. Liu, Y. Sun, 3D heterogeneous wetting microchannel surfaces for boiling heat transfer enhancement, Applied Surface Science, 457 (2018) 891-901.

[23] A. Surtaev, V. Serdyukov, A. Safonov, Characteristics of Boiling Heat Transfer on Hydrophobic Surface, The European Physical Journal Conferences, 196(54) (2019).

[24] P. Kangude, A. Srivastava, Understanding the growth mechanism of single vapor bubble on a hydrophobic surface: Experiments under nucleate pool boiling regime, International Journal of Heat and Mass Transfer, 154 (2020).

[25] X. Ma, P. Cheng, X. Quan, Simulations of saturated boiling heat transfer on bio-inspired two-phase heat sinks by a phase-change lattice Boltzmann method, Int. J. Heat Mass Transf., 127 (2018) 1013-1024.

[26] X. Chang, H. Huang, Y.-P. Cheng, X.-Y. Lu, Lattice Boltzmann study of pool boiling heat transfer enhancement on structured surfaces, International Journal of Heat and Mass Transfer, 139 (2019) 588-599.

[27] S. Chen, G.D. Doolen, Lattice Boltzmann method for fluid flows, Annual Review of Fluid Mechanics, 30 (1998) 329-364.

[28] C.K. Aidun, J.R. Clausen, Lattice-Boltzmann method for complex flows, Annual Review of Fluid Mechanics, 42 (2010) 439-472.

[29] Q. Li, K.H. Luo, Q.J. Kang, Y.L. He, Q. Chen, Q. Liu, Lattice Boltzmann methods for multiphase flow and phase-change heat transfer, Progress in Energy and Combustion Science, 52 (2016) 62-105.

[30] T. Krüger, H. Kusumaatmaja, A. Kuzmin, O. Shardt, G. Silva, E.M. Viggen, The Lattice Boltzmann Method - Principles and Practice, Springer Nature, 2017.

[31] S. Gong, P. Cheng, Numerical simulation of pool boiling heat transfer on smooth surfaces with mixed wettability by lattice Boltzmann method, Int. J. Heat Mass Transf., 80 (2015) 206-216.

[32] Q. Li, Y. Yu, P. Zhou, H.J. Yan, Enhancement of boiling heat transfer using hydrophilic-hydrophobic mixed surfaces: A lattice Boltzmann study, Applied Thermal Engineering, 132 (2018) 490-499.

[33] Y. Yu, Z.X. Wen, Q. Li, P. Zhou, H.J. Yan, Boiling heat transfer on hydrophilic-hydrophobic mixed surfaces: A 3D lattice Boltzmann study, Applied Thermal Engineering, 142 (2018) 846-854.

[34] W.X. Li, Q. Li, Y. Yu, Z.X. Wen, Enhancement of nucleate boiling by combining the effects of surface structure and mixed wettability: A lattice Boltzmann study, Applied Thermal Engineering, 180 (2020) 115849.

[35] J.S. Lee, J.S. Lee, Numerical study of hydrophobic-island shapes with patterned wettability for pool boiling, Applied Thermal Engineering, 127 (2017) 1632-1641.

[36] X. Ma, P. Cheng, 3D simulations of pool boiling above smooth horizontal heated surfaces by a phase-change lattice Boltzmann method, International Journal of Heat and Mass Transfer, 131 (2019) 1095-1108.

[37] Y.H. Qian, D. D'Humières, P. Lallemand, Lattice BGK Models for Navier-Stokes Equation, Europhysics Letters (EPL), 17(6) (1992) 479-484.

[38] S. Chen, H. Chen, D. Martnez, W. Matthaeus, Lattice Boltzmann model for simulation of magnetohydrodynamics, Phys Rev Lett, 67(27) (1991) 3776-3779.

[39] P. Lallemand, L.S. Luo, Theory of the lattice boltzmann method: dispersion, dissipation, isotropy, galilean invariance, and stability, Phys Rev E Stat Phys Plasmas Fluids Relat Interdiscip Topics, 61(6 Pt A) (2000) 6546-6562.

[40] Q. Li, D.H. Du, L.L. Fei, K.H. Luo, Three-dimensional non-orthogonal MRT pseudopotential lattice Boltzmann model for multiphase flows, Computers & Fluids, 186 (2019) 128-140.

[41] Q. Li, Q.J. Kang, M.M. Francois, Y.L. He, K.H. Luo, Lattice Boltzmann modeling of boiling heat transfer: The boiling curve and the effects of wettability, Int. J. Heat Mass Transf., 85 (2015) 787-796.

[42] Z. Guo, C. Shu. Lattice Boltzmann Method and Its Applications in Engineering, World Scientific, 2013.

[43] X. Shan, Pressure tensor calculation in a class of nonideal gas lattice Boltzmann models, Phys Rev E Stat Nonlin Soft Matter Phys, 77(6 Pt 2) (2008) 066702.

[44] Q. Li, K.H. Luo, X.J. Li, Lattice Boltzmann modeling of multiphase flows at large density ratio with an improved pseudopotential model, Phys Rev E Stat Nonlin Soft Matter Phys, 87(5) (2013) 053301.

[45] P. Yuan, L. Schaefer, Equations of state in a lattice Boltzmann model, Physics of Fluids, 18(4) (2006).

[46] R.B. Bird, W.E. Stewart, E.N. Lightfoot, Transport Phenomena, 2nd ed., John Wiley & Sons, Inc., 2001.

[47] Q. Li, P. Zhou, H.J. Yan, Improved thermal lattice Boltzmann model for simulation of liquid-vapor phase change, Phys. Rev. E, 96 (2017) 063303.

[48] N.R. Koosukuntla, Towards development of a multiphase simulation model using Lattice Boltzmann Method (LBM), Master's thesis, University of Toledo, Toledo, 2011.

[49] Y.L. He, Y. Wang, Q. Li, Lattice Boltzmann Method: Theory and Applications, Science, Beijing, (2009).

[50] Q. Zou, X. He, On pressure and velocity boundary conditions for the lattice Boltzmann BGK model, Phys. Fluids, 9(6) (1997) 1591-1598.

[51] M. Takeyama, T. Kunugi, Flow behavior around single nucleate boiling bubble quantitatively grasped by particle tracking visualization, International Journal of Multiphase Flow, 129 (2020).

[52] B. Qi, J. Wei, X. Wang, J. Zhao, Influences of wake-effects on bubble dynamics by utilizing micro-pin-finned surfaces under microgravity, Applied Thermal Engineering, 113 (2017) 1332-1344.

[53] S. Gong, P. Cheng, Two-dimensional mesoscale simulations of saturated pool boiling from rough surfaces. Part II: Bubble interactions above multi-cavities, Int. J. Heat Mass Transf., 100 (2016) 938-948.